Supplementary Materials for

Temperature Induces Brain-intake Shift of Recombinant High-density Lipoprotein after Traumatic Brain Injury

Authors

Jialin Huang [1, 2]†, Yidong Peng [1, 2]†, Xin Wang [4]†, Xiaokun Gu[1, 2]†, Yao Yi [2, 3]†, Wenye Wang [1, 2], Zhenghui He [1, 2], Zixuan Ma [1, 2], Qiyuan Feng [1, 2], Wenlan Qi [1,2], Jiyuan Hui [1], Ru Gong [1], Weiji Weng [1, 2], Gan Jiang [5], Yingwei Gao[1, 2], Yong Lin[1, 2], Jin Li [3], Jiyao Jiang [1, 2]*, Junfeng Feng [1, 2]**

Affiliations

[1]Brain Injury Center, Department of Neurosurgery, Ren Ji Hospital, Shanghai Jiao Tong University School of Medicine, Shanghai 200127, China.

[2]Shanghai Institute of Head Trauma, Shanghai 200127, China.

[3]Department of Ophthalmology, Ren Ji Hospital, Shanghai Jiao Tong University School of Medicine, Shanghai 200127, China.

[4]Department of Anesthesiology, Ren Ji Hospital, Shanghai Jiao Tong University School of Medicine, Shanghai 200127, China.

[5]Department of Pharmacology and Chemical Biology Shanghai Universities Collaborative Innovation Center for Translational Medicine Shanghai Jiao Tong University School of Medicine, Shanghai 200025, China

†: These five authors contributed equally to this work and should be considered co-first authors.

*Corresponding Author: Junfeng Feng, fengjfmail@163.com; Jiyao Jiang, jiyaojiang@126.com; Jin Li, lijinmpa@163.com

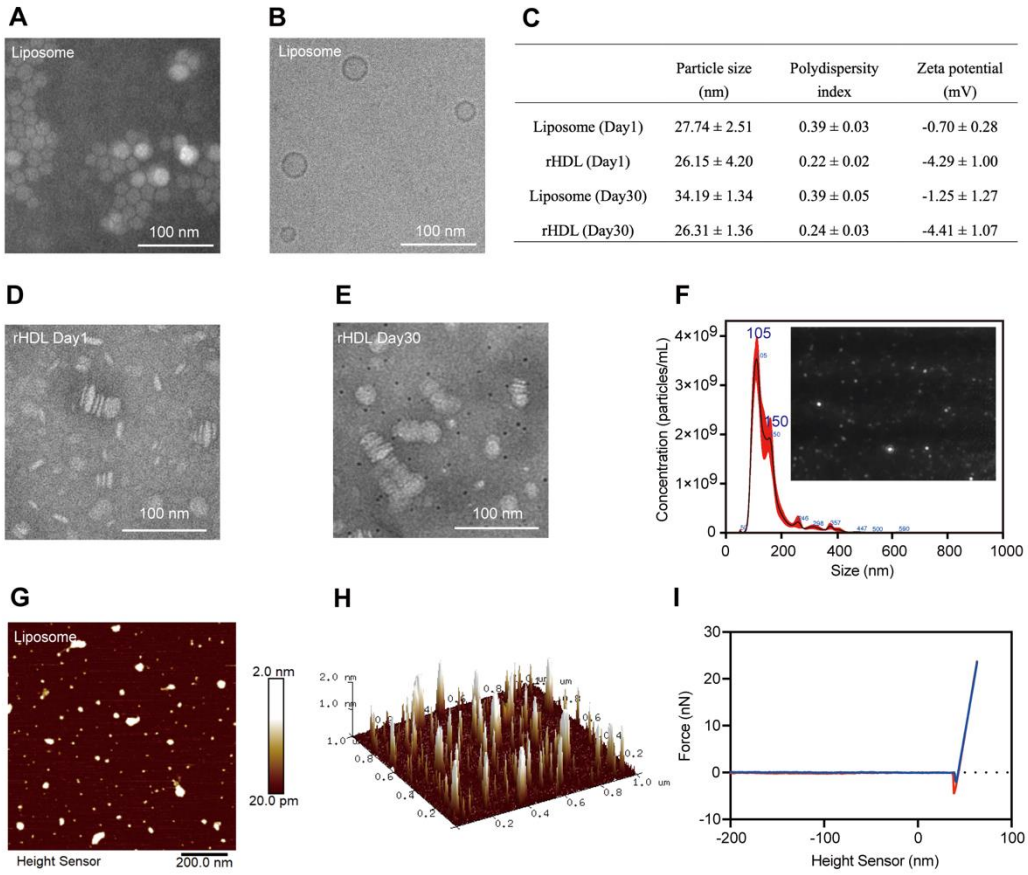

	Particle size (nm)	Polydispersity index	Zeta potential (mV)
Liposome (Day1)	27.74 ± 2.51	0.39 ± 0.03	-0.70 ± 0.28
rHDL (Day1)	26.15 ± 4.20	0.22 ± 0.02	-4.29 ± 1.00
Liposome (Day30)	34.19 ± 1.34	0.39 ± 0.05	-1.25 ± 1.27
rHDL (Day30)	26.31 ± 1.36	0.24 ± 0.03	-4.41 ± 1.07

Figure S1. Characterization of liposome. (A, B) Morphology and particle size of liposome under transmission electron microscope (A) and cryoelectron microscopy (B). Scale bar, 100 nm. (C) Particle characterization of liposome and rHDL analyzed by dynamic light scattering (DLS) via Zetasier. Data represented as mean ± SD ($n \geq 3$). (D, E) Morphology and particle size of rHDL at day 1 (D) and day 30 (E) by transmission electron microscopy. (F) Particle concentration of liposome obtained by NanoSight NS300. (G) The topographic images of liposome under atom force microscopy. Scale bar, 200 nm. (H) The three-dimensional projections of liposome under atom force microscopy. (I) The force curves of liposome under atom force microscopy. Blue lines refer to the approaching stage and red lines refer to the retracing stage.

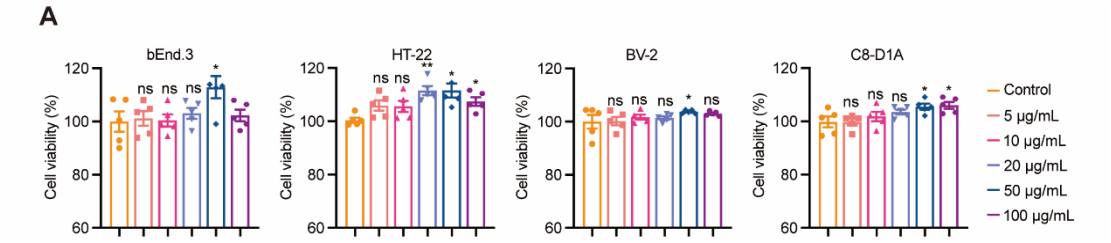

Figure S2. rHDL did not affect the cell viability of bEnd.3, HT-22, BV-2 and C8-D1A cells. bEnd.3, HT-22, BV-2 and C8-D1A cells were incubated with various concentrations of rHDL (0, 5, 10, 20, 50 and 100 μg/mL) for 12 h to investigate the cytotoxicity. The control group was defined as 100%. Data represented as mean ± SD ($n \geq 3$ per group). *$p < 0.05$, **$p < 0.01$, ***$p < 0.001$, ****$p < 0.0001$. NS: nonsignificant. Comparing the data with the control group. The significance of the differences was evaluated using one-way ANOVA with Tukey's multiple-comparisons test.

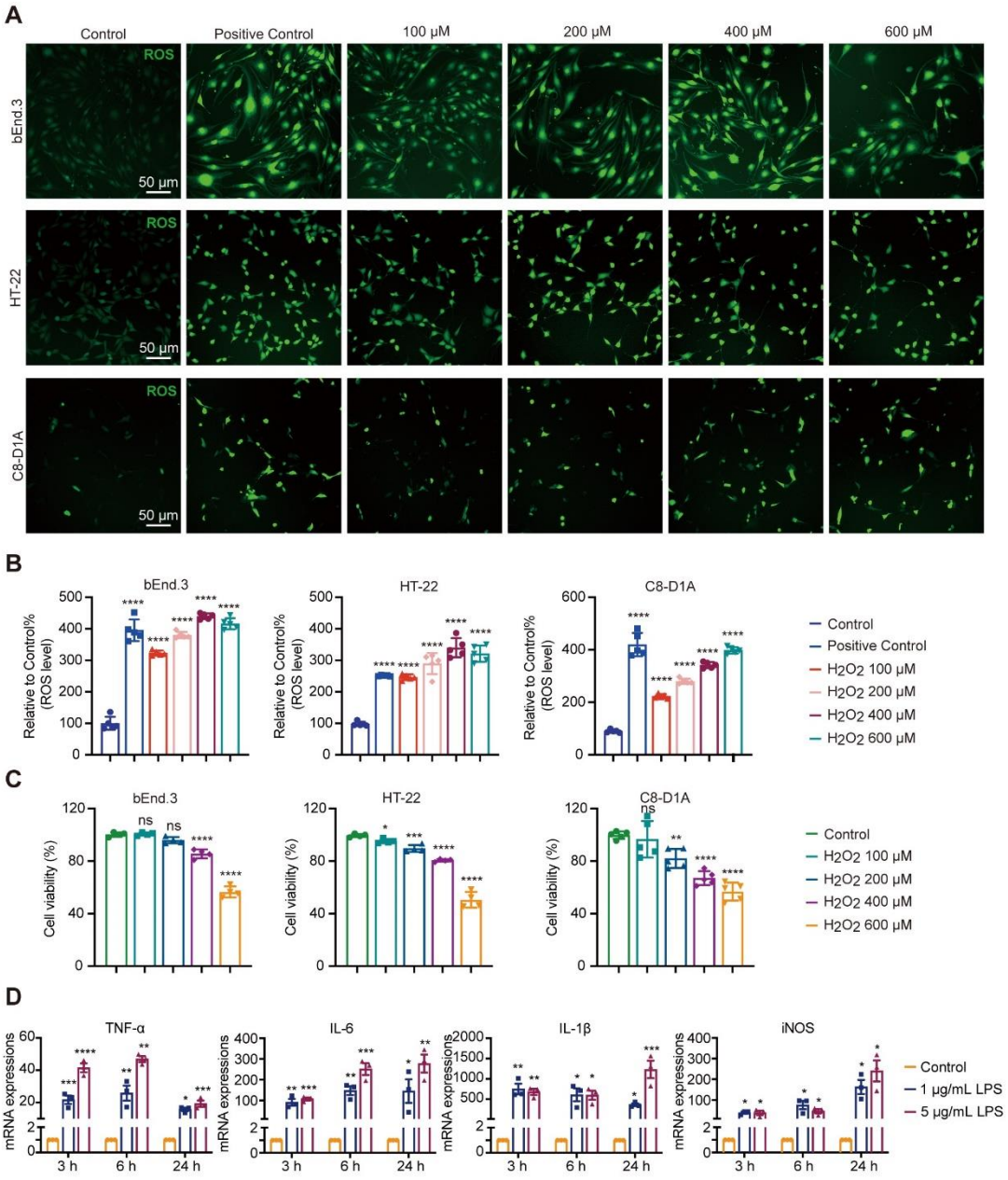

50

51 **Figure S3. Oxidative stress and inflammation models were established *in vitro*.** (A)
52 Reactive oxygen species (ROS) production in the bEnd.3, HT-22, and C8-D1A cells
53 after incubating with various concentrations of H_2O_2 (0, 100, 200, 400 and 600 μM) for
54 12 h. Green: ROS. Scale bar: 50 μm. (B) Semi-quantitative intracellular ROS levels by
55 ImageJ. The ROS level in the control group was defined as 100%. (C) bEnd.3, HT-22,
56 and C8-D1A cells were incubated with various concentrations of H_2O_2 (0, 100, 200,
57 400 and 600 μM) for 12 h to investigate cytotoxicity. The control group was defined as
58 100%. (D) BV-2 cells were treated with 1 μg/mL and 5 μg/mL LPS for 3 h, 6 h and 24

h. The mRNA levels of TNF-α, IL-6, IL-1β, and iNOS were determined by qRT-PCR. Data are reported as mean ± SD (n ≥ 3 per group). *p < 0.05, **p < 0.01, ***p < 0.001, ****p < 0.0001. NS: nonsignificant. Comparing the data with the control group. The significance of the differences was evaluated using one-way ANOVA with Tukey's multiple-comparisons test.

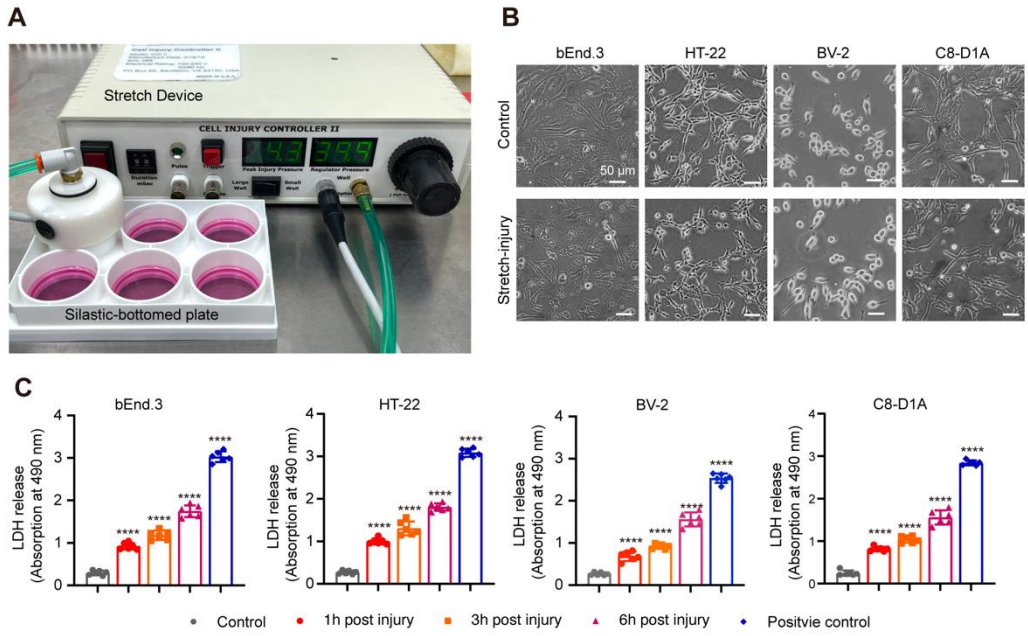

Figure S4. Stretch-injury models were established *in vitro*. (A) Illustration of cell stretch-injury model. (B) Cell morphology before and after stretch injury. (C) LDH release levels at different time points after stretch injury. Data were represented as mean ± SD (n ≥ 3 per group). *p < 0.05, **p < 0.01, ***p < 0.001, ****p < 0.0001. Comparing data with the control group. The significance of the differences was evaluated using one-way ANOVA with Tukey's multiple-comparisons test.

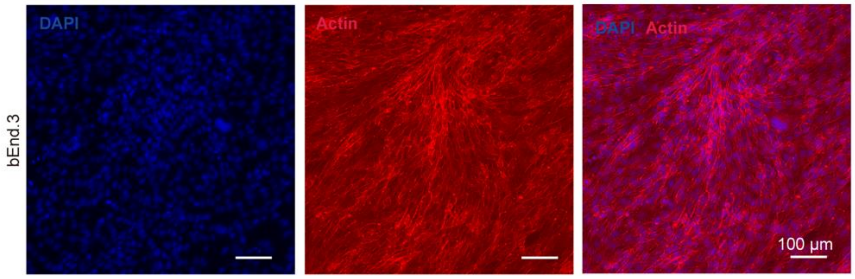

Figure S5. Confirming the *in vitro* BBB model integrity by phalloidin staining. Fluorescence images of bEnd.3 cell monolayer after 7-day cell culture in transwell upper chamber. The nuclei and actin were stained with DAPI and Rhodamine-Phalloidin, respectively. Scale bar, 100 μm.

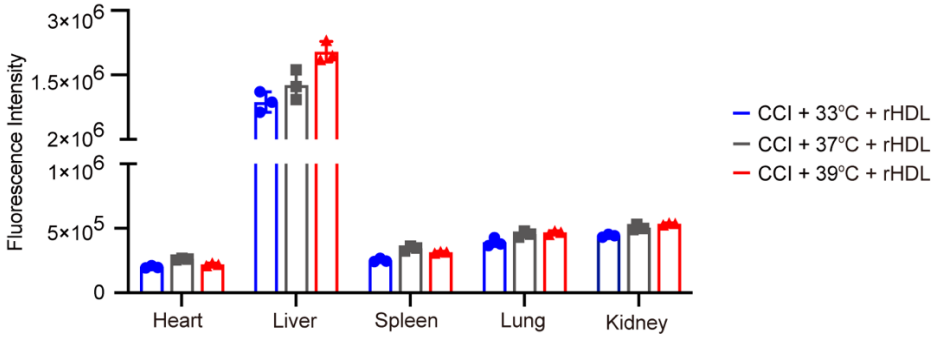

Figure S6. Quantitative analysis of ex vivo organ in the CCI mice. Quantitative analysis of ex vivo organ accumulation of DiR-labelled rHDL at 3 h post-injection in the CCI mice treated with 33ºC, 37ºC, and 39ºC, respectively. Data were represented as mean ± SD ($n \geq 3$ per group). *$p < 0.05$, **$p < 0.01$, ***$p < 0.001$, ****$p < 0.0001$. Comparing data with the normothermia group (37ºC). The significance of the differences was evaluated using one-way ANOVA with Tukey's multiple-comparisons test.

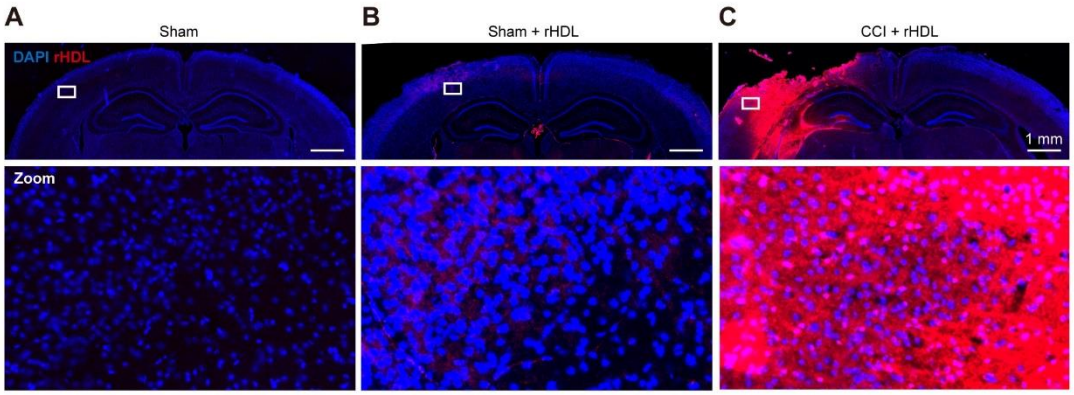

Figure S7. Brain distribution of DiI-labeled rHDL at 3 h post-injection in the mice from (A) sham group without rHDL injection, (B) sham group with rHDL injection and (C) CCI group with rHDL injection. Scale bar, 1mm.

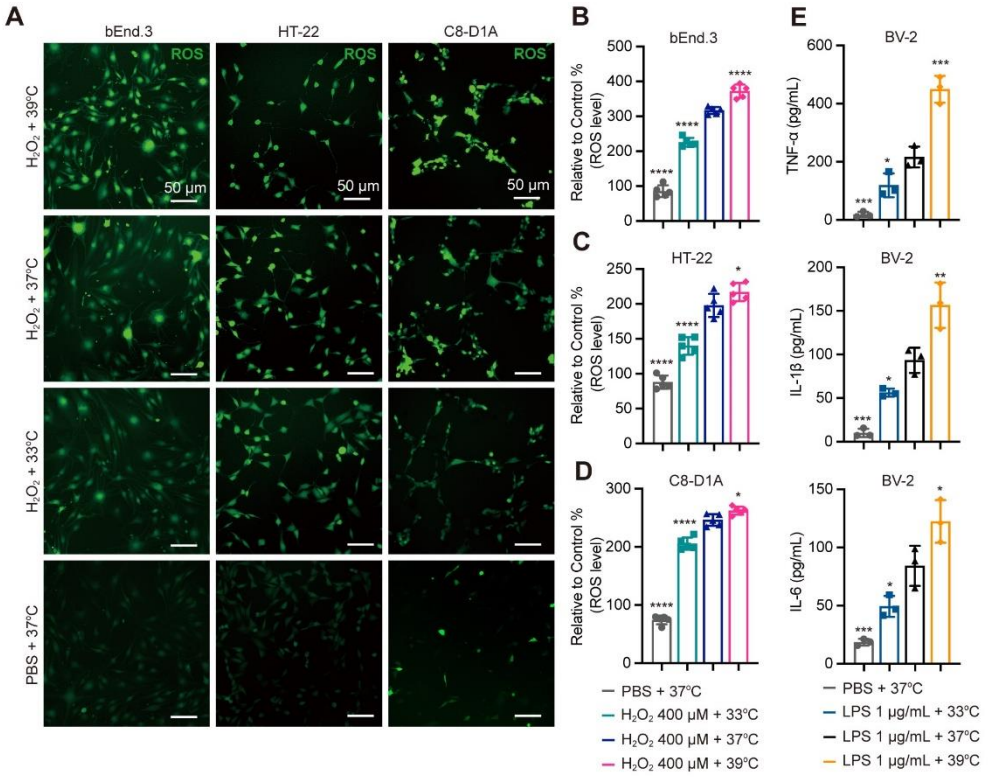

Figure S8. Temperature affected the level of oxidative stress and inflammation response in bEnd.3, HT-22, C8-D1A and BV-2 cells. (A) ROS production in bEnd.3, HT-22, and C8-D1A cells after incubating with 400 μM H_2O_2 for 12 h before incubating under the temperature of 33°C, 37°C and 39°C for 3 h. Green: ROS. Scale bar: 50 μm.

(B-D) Semi-quantitative intracellular ROS levels by ImageJ. The ROS level in the control group was defined as 100%. (E) Effects of different temperatures on cytokine production by LPS-reactive microglia. BV-2 were cultured with 1 μg/mL LPS for 3 h before incubating under temperatures of 33°C, 37°C and 39°C for 3 h. Data represented as mean ± SD (n ≥ 3 per group). *p < 0.05, **p < 0.01, ***p < 0.001, ****p < 0.0001. Comparing data with the normothermia group (37°C). The significance of the differences was evaluated using one-way ANOVA with Tukey's multiple-comparisons test.

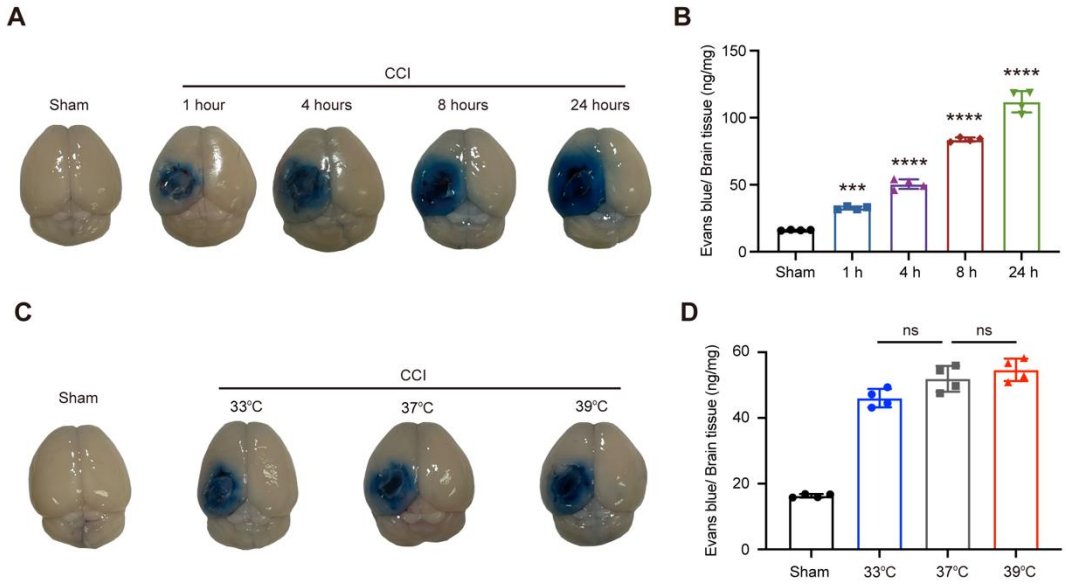

Figure S9. CCI injury resulted in a progressive increase in the permeability of BBB within 24 hours, which was not significantly affected by temperature. (A) Images of EB-labeled brain of healthy mice or CCI mice by EB penetration assay. EB was intravenously injected into healthy mice or mice with CCI at different time points after injury. Two hours following EB administration, the brains were excised and photographed. (B) Quantitative analysis of EB leakage at different time points. (C) Images of EB-labeled brain of CCI mice at 33°C, 37°C, and 39°C. EB was intravenously injected into mice suffering CCI and controlled temperature at 33°C, 37°C, and 39°C for 3 hours. (D) Quantitative analysis of EB leakage at different temperatures. Data were represented as mean ± SD (n ≥ 3 per group). *p < 0.05, **p < 0.01, ***p < 0.001,

****p < 0.0001. The significance of the differences was evaluated using one-way ANOVA with Tukey's multiple-comparisons test.

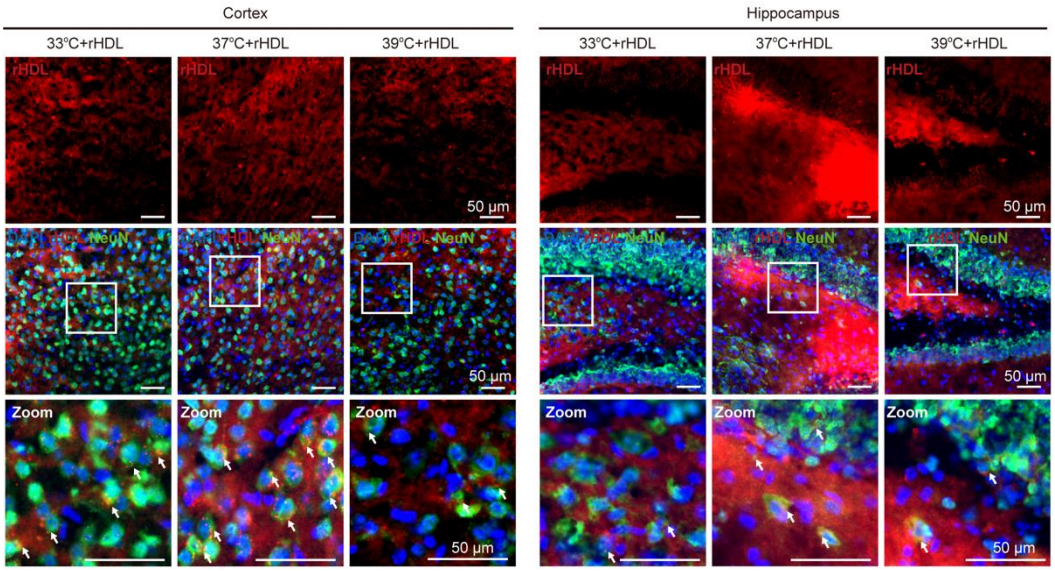

Figure S10. Both mild hypothermia and hyperthermia inhibited rHDL's uptake by injured neurons following TBI. Representative fluorescence images of DiI-labeled rHDL distribution in the injured cortex and hippocampus of C57BL/6 mice suffering CCI at 3 h after i.v. administration at 33°C, 37°C and 39°C, respectively. Green: NeuN+ neurons. Red: DiI-labeled rHDL. Blue: cell nuclei. Scale bar, 50 μm. The white arrow indicated the neurons that absorbed rHDL.

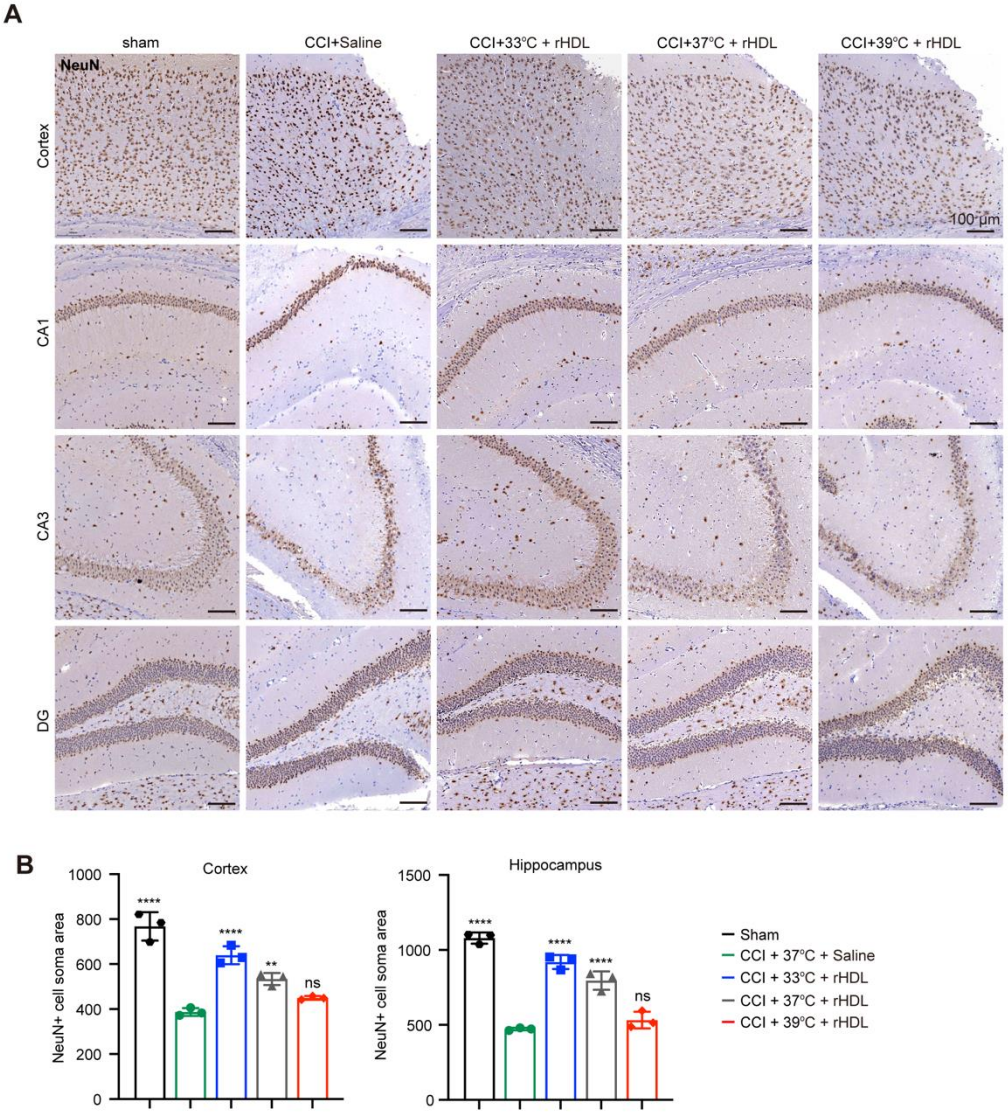

Figure S11. Temperature and rHDL affected neuron soma shrinking in CCI mice. (A) NeuN immunostaining in the cortex and hippocampus (CA1, CA3, DG) of CCI mice. Representative pictures from phase contrast microscope were shown. Scale bar, 100 μm. (B) Semi-quantitative analysis of NeuN+ area in the cortex and hippocampus with Image J software. Data represented as mean ± SD ($n \geq 3$ per group). *$p < 0.05$, **$p < 0.01$, ***$p < 0.001$, ****$p < 0.0001$. The significance of the differences was evaluated using one-way ANOVA with Tukey's multiple-comparisons test.

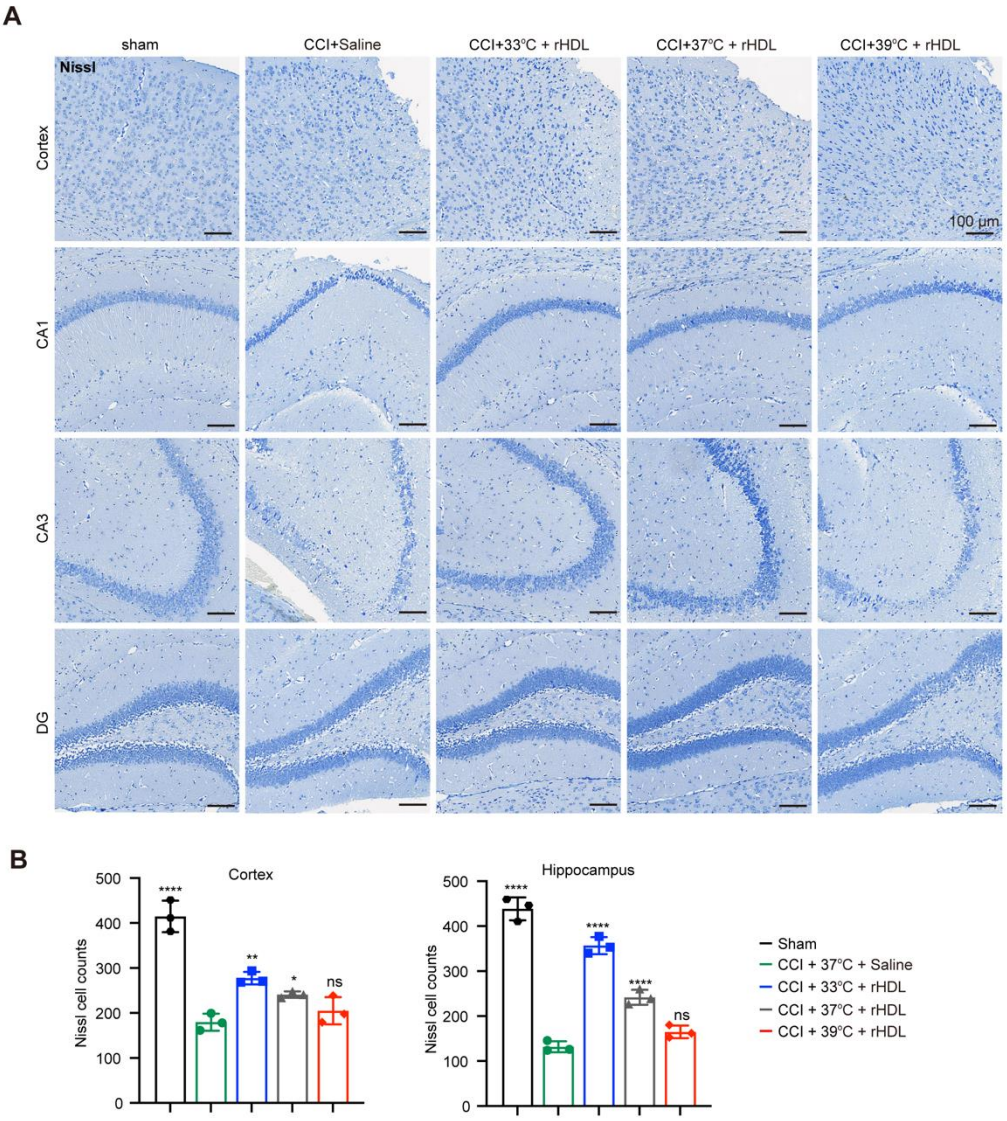

Figure S12. Temperature and rHDL affected neuron survival in CCI mice. (A) Nissl staining in the cortex and hippocampus (CA1, CA3, DG) of CCI mice. Representative pictures from the phase contrast microscope were shown. Scale bar, 100 μm. (B) Semi-quantitative analysis of nissl cells counts in the cortex and hippocampus with Image J software. Data represented as mean ± SD ($n \geq 3$ per group). *$p < 0.05$, **$p < 0.01$, ***$p < 0.001$, ****$p < 0.0001$. The significance of the differences was evaluated using one-way ANOVA with Tukey's multiple-comparisons test.

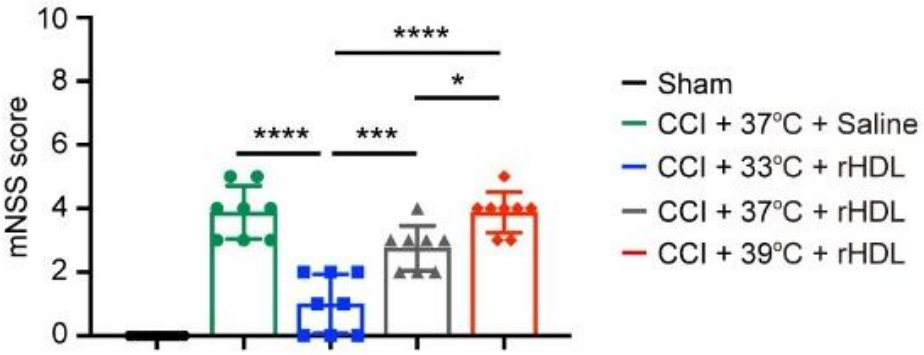

149

150 **Figure S13. Temperature and rHDL affected mNSS score of CCI mice.** mNSS score
151 of CCI mice with different treatments. Data represented as mean ± SD (n = 8 per group).
152 *p < 0.05, **p < 0.01, ***p < 0.001, ****p < 0.0001. The significance of the differences
153 was evaluated using one-way ANOVA with Tukey's multiple-comparisons test.

154

155

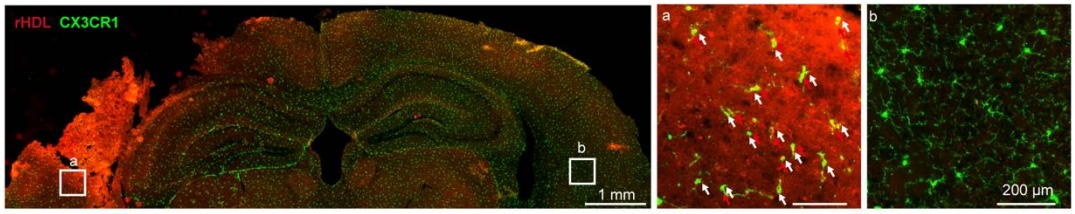

156

157 **Figure S14. The reactivity of microglia and their uptake of rHDL in the ipsilateral**
158 **and contralateral side of the brain in CCI model mice.** Representative fluorescence
159 images of DiI-labeled rHDL distribution in the ipsilateral (a) and contralateral side (b)
160 of the brain of CX3CR1-GFP mice suffering CCI at 3 h after i.v. administration. Green:
161 GFP-labeled microglia. Red: DiI-labeled rHDL. The white arrow indicated the
162 microglia that absorbed rHDL. The red arrow indicated reactive microglia with the
163 shape of an amoeboid.

164

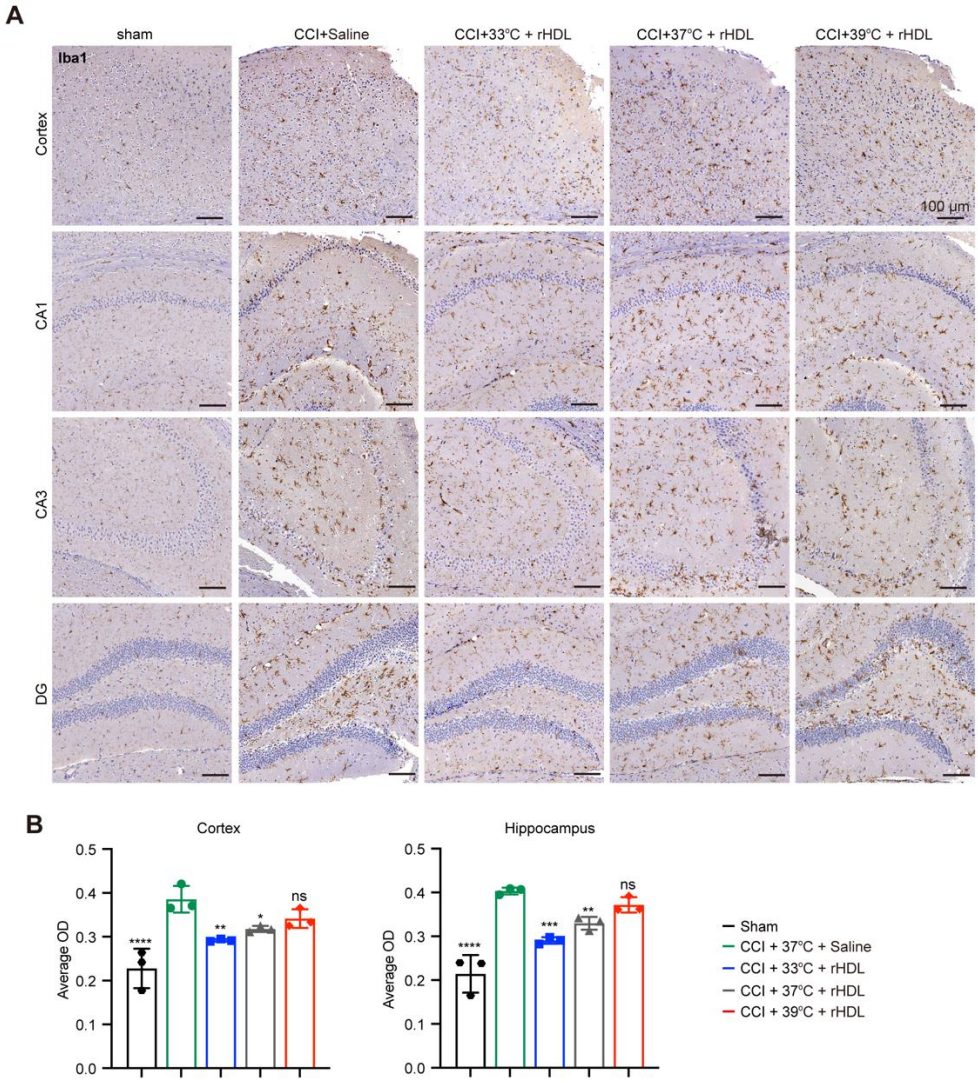

165

166 **Figure S15. Temperature and rHDL affected the reactivity of microglia in CCI**
167 **mice.** (A) Iba1 immunostaining in the cortex and hippocampus (CA1, CA3, DG) of
168 CCI mice. Representative pictures from phase contrast microscope were shown. Scale
169 bar, 100 μm. (B) Semi-quantitative analysis of reactive microglia in cortex and
170 hippocampus with Image J software. Data represented as mean ± SD ($n \geq 3$ per group).
171 *$p < 0.05$, **$p < 0.01$, ***$p < 0.001$, ****$p < 0.0001$. The significance of the differences
172 was evaluated using one-way ANOVA with Tukey's multiple-comparisons test.

173

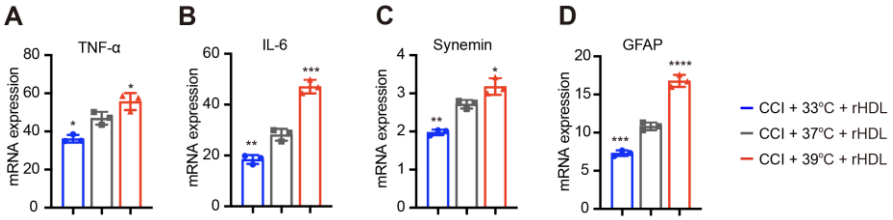

Figure S16. The expression level of reactive markers in glial cells was temperature-dependent following CCI. Effects of different temperatures on the expression level of reactive markers of microglia (TNF-α and IL-6) and astrocytes (Synemin and GFAP). Data represented as mean ± SD (n ≥ 3 per group). *p < 0.05, **p < 0.01, ***p < 0.001, ****p < 0.0001. Comparing data with the normothermia group (37°C). The significance of the differences was evaluated using one-way ANOVA with Tukey's multiple-comparisons test.

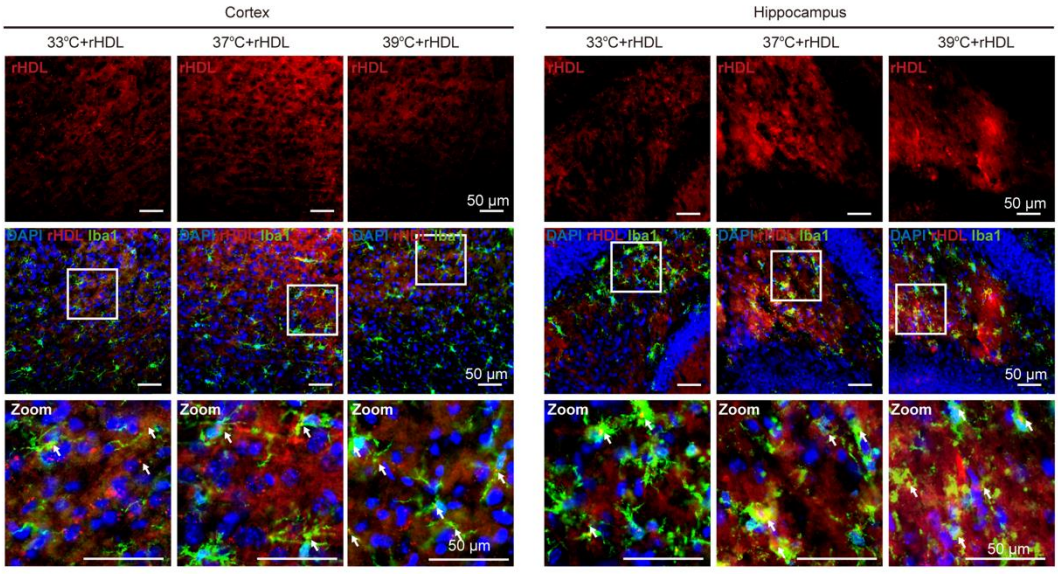

Figure S17. Mild hypothermia inhibited while hyperthermia promoted rHDL's uptake by reactive microglia following TBI. Representative fluorescence images of DiI-labeled rHDL distribution in the injured cortex and hippocampus of C57BL/6 mice suffering CCI at 3 h after i.v. administration at 33°C, 37°C and 39°C, respectively. Green: Iba1+ microglia. Red: DiI-labeled rHDL. Blue: cell nuclei. Scale bar, 50 μm. The white arrow indicated the microglia that absorbed rHDL.

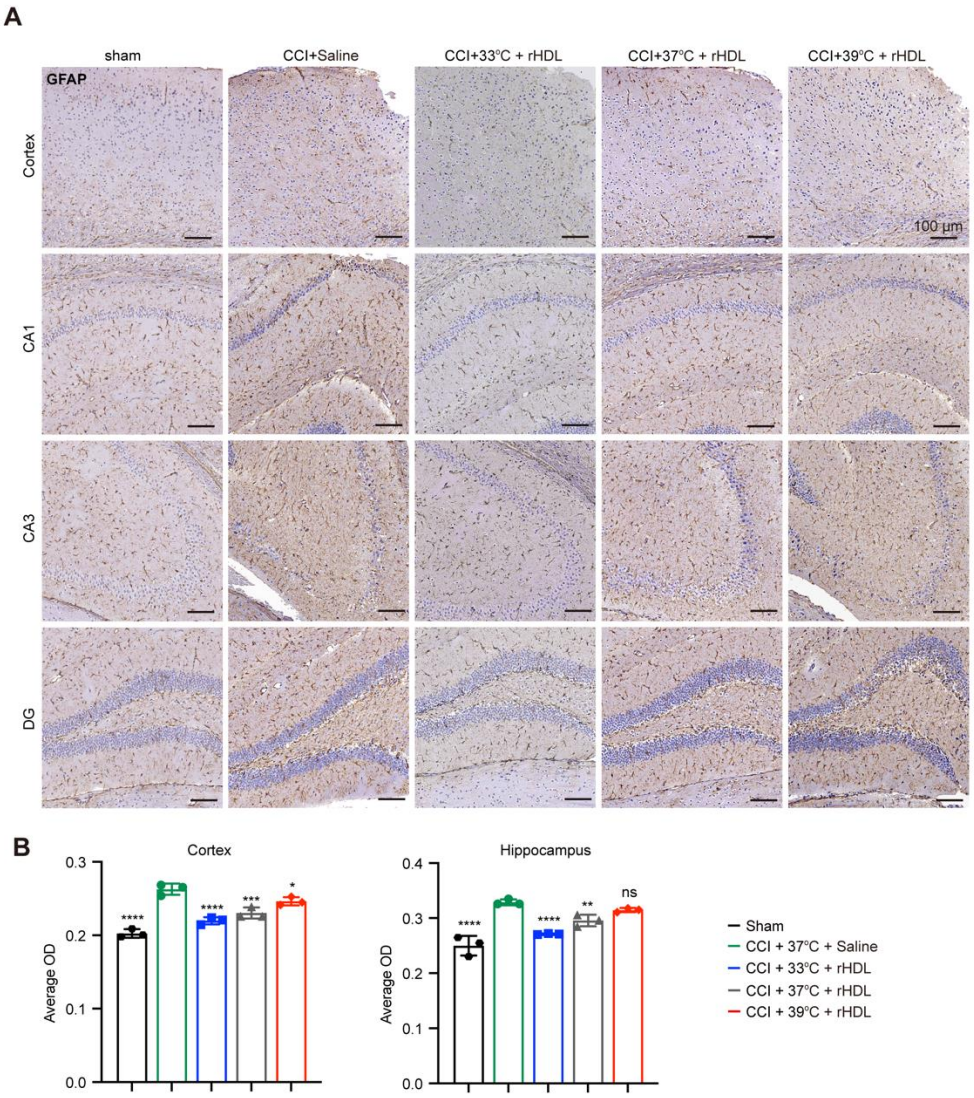

Figure S18. Temperature and rHDL affected the activation of astrocytes in CCI mice. (A) GFAP immunostaining in the cortex and hippocampus (CA1, CA3, DG) of CCI mice. Representative pictures from phase contrast microscope were shown. Scale bar, 100 μm. (B) Semi-quantitative analysis of activated astrocytes in cortex and hippocampus with Image J software. Data represented as mean ± SD ($n \geq 3$ per group). *$p < 0.05$, **$p < 0.01$, ***$p < 0.001$, ****$p < 0.0001$. The significance of the differences was evaluated using one-way ANOVA with Tukey's multiple-comparisons test.

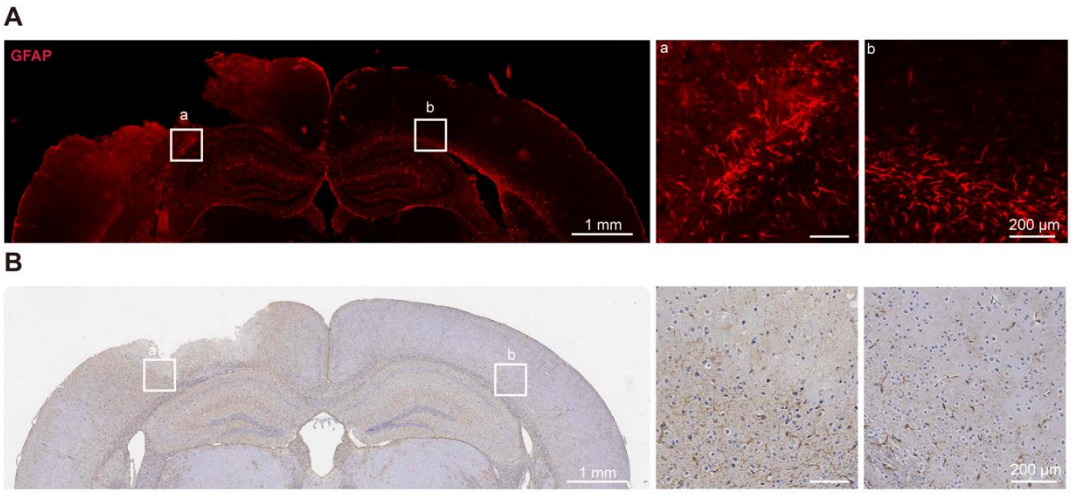

Figure S19. The activation of astrocytes in the ipsilateral and contralateral side of the brain in CCI model mice. Immunofluorescent (A) and Immunohistochemical (B) analysis of GFAP expression in the injured (a) and contralateral (b) cortex of CCI model mice.

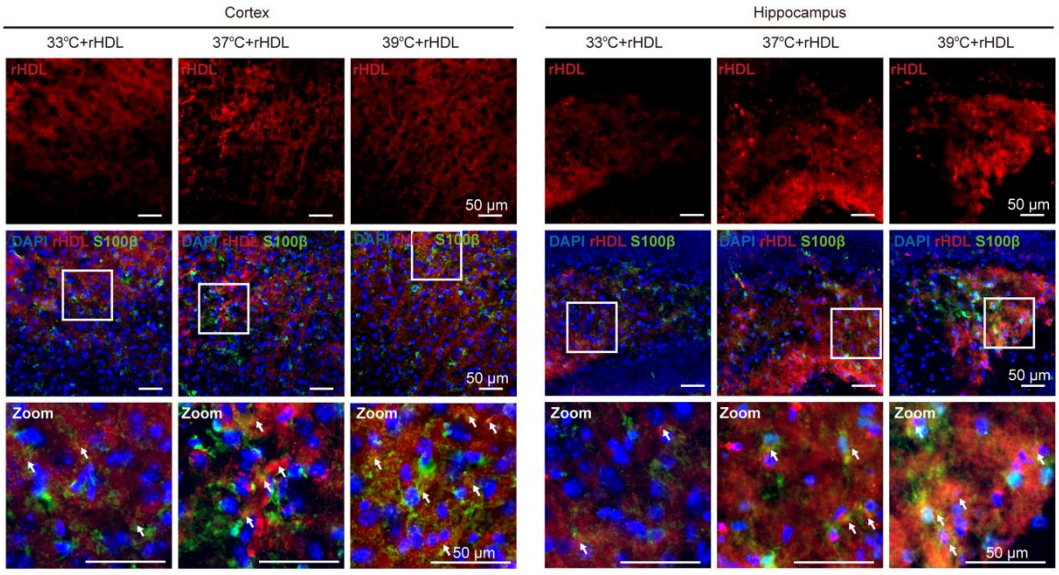

Figure S20. Mild hypothermia inhibited while hyperthermia promoted rHDL's uptake by injured astrocytes following TBI. Representative fluorescence images of DiI-labeled rHDL distribution in the injured cortex and hippocampus of C57BL/6 mice suffering CCI at 3 h after i.v. administration at 33°C, 37°C and 39°C, respectively. Green: S100β+ astrocytes. Red: DiI-labeled rHDL. Blue: cell nuclei. Scale bar, 50 μm. The white arrow indicated the microglia that absorbed rHDL.

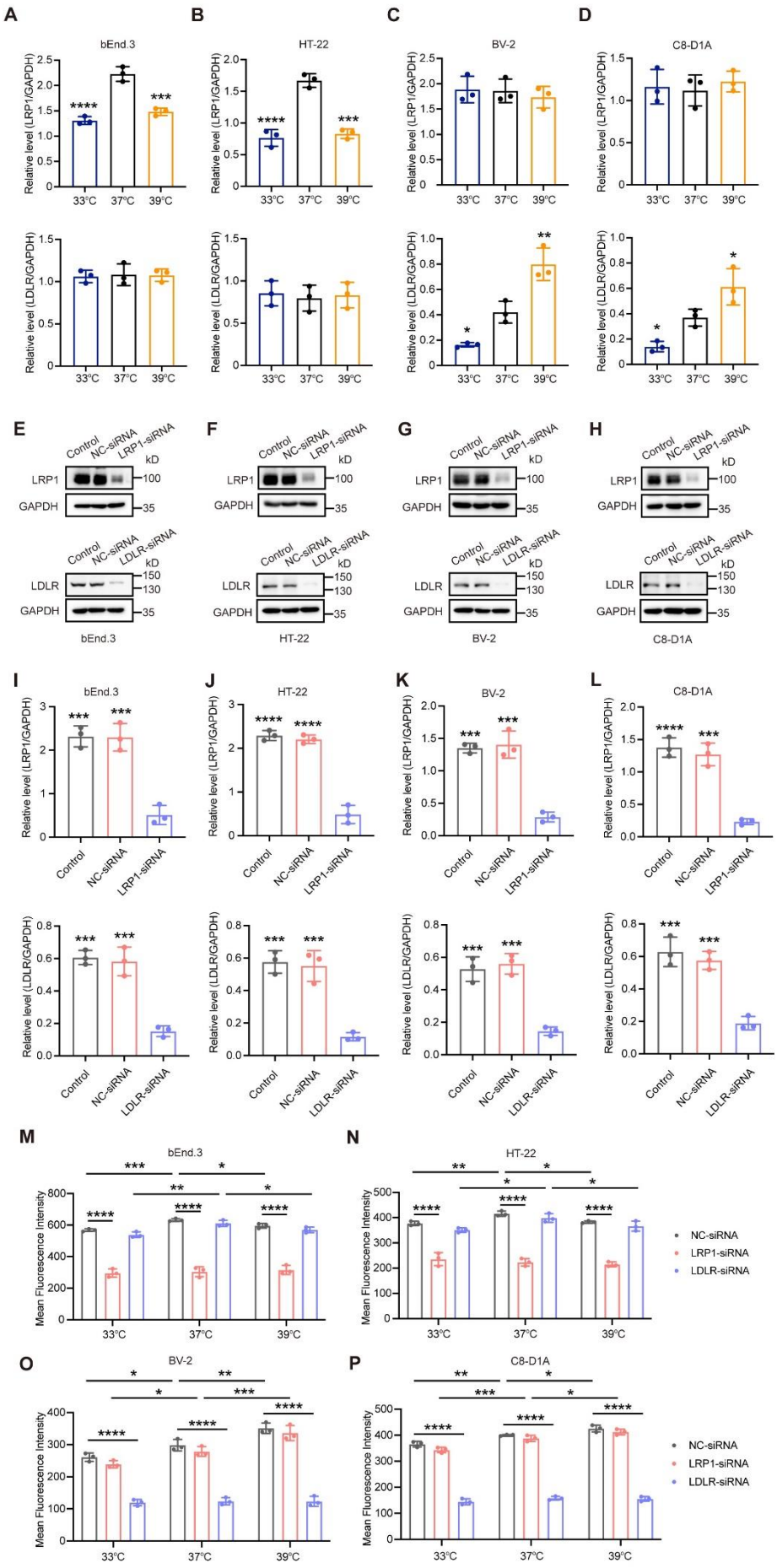
A
B
C
D
bEnd.3
HT-22
BV-2
C8-D1A
Relative level (LRP1/GAPDH)
Relative level (LDLR/GAPDH)
33°C
37°C
39°C
E
F
G
H
Control
NC-siRNA
LRP1-siRNA
LDLR-siRNA
kD
LRP1
LDLR
GAPDH
100
150
130
35
I
J
K
L
M
N
O
P
Mean Fluorescence Intensity
NC-siRNA
LRP1-siRNA
LDLR-siRNA

Figure S21. Temperature-induced modulation of rHDL brain uptake through the regulation of LDLR and LRP1 stability in brain cells. (A-D) The quantification of LDLR and LRP1 protein expression from injured (A) bEnd.3, (B) HT-22, (C) BV-2 and (D) C8-D1A with 33°C, 37°C and 39°C treatments. Normalized LRP1 and LDLR to corresponding loading control were summarized for three independent trials. (E-H) Western blots analysis showed the protein expression of LRP1 and LDLR after negative control (NC) or LRP1 and LDLR siRNA transfection in injured (E) bEnd.3, (F) HT-22, (G) BV-2 and (H) C8-D1A cells. GAPDH was used as the loading control. (I-L) The quantification of Western blots of (E-H). (M-P) Semi-quantitative fluorescent analysis of cellular uptake of DiI-labeled rHDL in injured (M) bEnd.3, (N) HT-22, (O) BV-2 and (P) C8-D1A cells at 33°C, 37°C and 39°C, respectively. All Data represented as mean ± SD (n = 3 per group). *$p < 0.05$, **$p < 0.01$, ***$p < 0.001$, ****$p < 0.0001$. The significance of the differences was evaluated using one-way ANOVA with Tukey's multiple-comparisons test.

Table S1. List of primers used in this study.

Gene	Direction	Sequence	Accession
TNF-α	Forward	CAGGCGGTGCCTATGTCTC	NM_013693
TNF-α	Reverse	CGATCACCCCGAAGTTCAGTAG	
IL-6	Forward	CTGCAAGAGACTTCCATCCAG	NM_031168
IL-6	Reverse	AGTGGTATAGACAGGTCTGTTGG	
IL-1β	Forward	GAAATGCCACCTTTTGACAGTG	NM_008361
IL-1β	Reverse	TGGATGCTCTCATCAGGACAG	
iNOS	Forward	ACATCGACCCGTCCACAGTAT	NM_010927
iNOS	Reverse	CAGAGGGGTAGGCTTGTCTC	
Synemin	Forward	TGAAAACGTGCCACAAGAGC	NM_207663
Synemin	Reverse	CGAGGCCGAGCTGTGATTTA	
GFAP	Forward	CCCTGGCTCGTGTGGATTT	NM_001131020
GFAP	Reverse	GACCGATACCACTCCTCTGTC	

Table S2. Roughness, Young's Modulus and Adhesion forces of the nanoparticles.

	Roughness (Ra/Rq)	Young's Modulus (Mpa)	Adhesion forces (nN)
Liposome	0.64 ± 0.04	339.67 ± 122.66	3.95 ± 0.43
rHDL	0.41 ± 0.01	848.25 ± 105.65	18.11 ± 1.37

[a] Values are mean ± SD of at least three different preparations.